



Improving low-temperature CS₂ conversion for the Claus process by using La (III)-doped nanofibrous TiO₂ xerogel

Ruohong Sui, Christopher B. Lavery, Dao Li, Connor E. Deering, Nancy Chou, Norman I. Dowling, Robert A. Marriott*

Chemistry Department, University of Calgary, 2500 University Drive, Northwest Calgary, Alberta, T2L 4N1, Canada

ARTICLE INFO

Keywords:

Macropores
Lewis-base
Claus process
Sol-gel
Self-assembly
Nanofibrous xerogel
La-doped titania
sulfur fouling

ABSTRACT

Not only do the natural gas and petroleum industries face the challenge of stringent sulfur compound emission limits, but it is also important to use new technologies to reduce the carbon footprint and improve energy efficiency. Herein this research is aimed at developing a new generation of catalysts that can potentially decrease the reaction temperature of Claus catalytic converters (used to convert sulfur compounds to elemental sulfur), and also reduce the amount of catalyst. There are two factors that affect the performance of the conventional Claus catalysts. First, the conventional metal oxide catalysts suffer from ageing, trapped liquid sulfur fouling in the mesopores and high steady-state concentration of surface sulfate, which reduce the number of active sites for CS₂ conversion. Therefore, the industry has to pay the price for a high reaction temperature to maintain a satisfactory CS₂ conversion, while sacrificing Claus conversion (2H₂S + SO₂). Second, Al₂O₃ and TiO₂ are widely used for Claus reactions; nevertheless, they are not active for conversion of CS₂ at lower temperatures. In this context, our approach in this research is using nanofibrous La(III)-doped TiO₂ as a new Claus catalyst. La(III) is incorporated into titanium-oxo-acetate complexes via a one-pot sol-gel process, followed by calcination to form a nanofibrous xerogel. Because the nanofibers join together to form a connected network, the xerogel monolith has large macroporosity and exhibits a low density. The exterior surface of the nanofibers, which makes a large contribution to the surface area, remains intact under harsh conditions and thereby is accessible by the reactants. In addition, the La(III) doped TiO₂ exhibits more Lewis-base activity that is effective for CS₂ conversion. For comparison, TiO₂ xerogels were deposited with La(III) by means of an impregnation method and also tested for Claus reaction activity; however, the catalytic performance of this material was reduced compared to the pure TiO₂ counterpart. On the basis of characterization studies on these catalysts, it is concluded that (i) a good distribution of La(III) in TiO₂ matrix and (ii) the method of La(III) incorporation are important for CS₂ conversion.

1. Introduction

As a relatively clean energy resource, natural gas currently provides a significant proportion of the total energy consumed, worldwide. Also, with phasing out of coal power stations, more electricity generation will be powered by natural gas, further boosting natural gas consumption. However, many natural gas reservoirs around the world contain H₂S. In addition, crude oil refineries also need to handle H₂S produced from the hydrosulphurization process. Although other options are under development [1–3], H₂S is often removed by amine scrubbing followed by the modified Claus process [4]. In a Claus plant, H₂S first reacts with oxygen in a furnace to produce SO₂ and elemental sulfur (Eqs. (1) and (2)) at over 1273 K. The unreacted H₂S and SO₂ (limited by

equilibrium), together with by-products such as CS₂ and COS [5], are cooled and introduced into two or three converters using Al₂O₃ or TiO₂ as a catalyst. The forward modified Claus reaction (Eq. (3)) is favored at a lower temperature; however, a temperature above the sulfur dew point is necessary to keep the catalyst bed free from liquid elemental sulfur. In the industrial process the first converter is heated to 573–593 K, well above the sulfur dew point to destroy CS₂ (Eqs. (4) and (5)). This is because a lower reaction temperature dramatically decreases the catalytic CS₂ conversion. This is due to both poor activity for CS₂ conversion over the bare catalyst surface and poisoning by sulfur capillary condensation in the small pores of the traditional catalysts that significantly reduce the active surface area [6–8]. If the reaction temperature can be decreased by developing a new catalyst, which can

* Corresponding author.

E-mail address: rob.marriott@ucalgary.ca (R.A. Marriott).

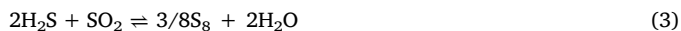
<https://doi.org/10.1016/j.apcatb.2018.09.027>

Received 9 July 2018; Received in revised form 5 September 2018; Accepted 9 September 2018

Available online 12 September 2018

0926-3373/ © 2018 Elsevier B.V. All rights reserved.

prevent surface fouling, both the energy efficiency and operation cost would be improved.



As the most studied metal oxides, TiO_2 are widely used as photocatalysts, semiconductors, biomaterials, and catalysts in the chemical and energy industries [9]. Its inherent shortcomings, such as relatively low thermal stability and a large band gap, have been improved by modification of TiO_2 using doping or deposition techniques [10]. Here doping refers to replacement of Ti(IV) in the bulk lattice by foreign elements, and deposition means a decoration of other materials on the surface of TiO_2 . La(III) has been investigated for the modification of TiO_2 by using sol-gel, co-precipitation, and impregnation methods [11]. The benefits of these modifications are plentiful, such as a stabilized anatase phase, a relatively persistent surface area at an elevated temperature, more favourable surface defects for catalysis activity, a reduced electron-hole pair recombination rate and a lower band gap in the visible light region for an improved photocatalytic activity [12,13].

Due to the large void space, nanofibrous metal oxides are attractive for adsorption/desorption, filtration, and catalytic processes when mass transfer is a bottleneck or fouling is problematic. However, the conventional industrial methods for preparing TiO_2 catalysts, including the benchmark photocatalyst Degussa P25, only produce spherical particles [14]. Among the methods for making nanofibers, the sol-gel approach is most promising because of its scalability and low-cost for production, although it will need a support for commercial deployment. A short hydrocarbon carboxylic acid, e.g., acetic acid, is used to direct an anisotropic growth of sol-gel nanostructures [15]. Calcination of these nanostructures results in formation of metal oxides, and the anisotropic features are desirably maintained. To date, TiO_2 and Al_2O_3 nanofibers, Zr(IV)/ TiO_2 nanotubes and Al_2O_3 nanoribbons have been prepared by using this approach [16–18]. In addition, the sol-gel co-processing of bi- or tri-metal precursors is a powerful tool for making hybrid metal oxides with a uniform distribution on a molecular scale [19]. Importantly, the nanofibers produced by this sol-gel process are bound together to form a stiff network, suitable for catalytic applications.

In this context, the main objective of this research is to develop a La(III)-doped fibrous TiO_2 catalyst and to test its performance for sulfur recovery at a lower temperature, because La(III) is known to stabilize TiO_2 crystalline phases and relatively inexpensive [20]. For comparison purposes, La(III)-deposited fibrous TiO_2 , non-modified fibrous TiO_2 , and conventional TiO_2 (composed of spherical particles) were also tested. Characterizations of both fresh and used catalysts are discussed for a better understanding of the CS_2 conversion reactions.

2. Methods

Safety note. Because the Claus experiments described here involved the use of toxic H_2S and SO_2 , a detector-equipped cabinet and a KOH caustic scrubbing system were used for the catalyst tests. These detectors are interfaced with air operated valves to halt gas flow if the concentration in the cabinet exceeds 5 ppmv.

2.1. Materials

97% Titanium isopropoxide ($\text{Ti}(\text{O}^i\text{Pr})_4$), 99.9% lanthanum acetate ($\text{La}(\text{OAc})_3$), 99.99% $\text{La}(\text{NO}_3)_3(\text{H}_2\text{O})_6$, and anhydrous heptanes (99%) were purchased from Sigma-Aldrich and were used without further purification. 99.7% acetic acid (HOAc) from Sigma-Aldrich was

dehydrated with molecular sieve 5 A for 24 h before use. All gases were obtained from Praxair (Canada) with a minimum purity of 99.999%, except 99.6% H_2S .

2.2. Catalyst preparation

In this study, spherical and fibrous TiO_2 catalysts have been prepared with a sol-gel method. Modification of TiO_2 with predetermined 4 wt.% La_2O_3 (within a typical range for TiO_2 modification) has been conducted by either one-pot-synthesis doping or an impregnation deposition method.

Synthesis of nanofibrous La(III) doped TiO_2 (La(III)/ TiO_2 -dop). A 2 L flask, equipped with a magnetic stirrer, a heating mantle and a reflux condenser, was used as a sol-gel reactor. In a typical experiment, 400 mL of heptane and 363.3 g of HOAc and 8.34 g of $\text{La}(\text{OAc})_3 \cdot 1.5\text{H}_2\text{O}$ were added sequentially to the flask and the mixture was heated to 333 K with stirring. After $\text{La}(\text{OAc})_3$ was dissolved, 329.3 g of $\text{Ti}(\text{O}^i\text{Pr})_4$ was added into the flask. When gelation occurred within 1 day, the gel was aged for two more days at the reaction temperature, and the resulting material was dried under vacuum at $T = 353$ K for 12 h.

Synthesis of nanofibrous TiO_2 (TiO_2 -nf). The synthesis method for this material has been described previously [15]. The only difference between the doped and the non-doped TiO_2 synthesis was that La(III) precursor was not used in the non-doped material.

Synthesis of conventional TiO_2 (TiO_2 -ns). The synthesis method has been described previously [15]. The only synthesis difference between TiO_2 -nf and TiO_2 -ns was different molar ratios (r) of HOAc vs. $\text{Ti}(\text{O}^i\text{Pr})_4$. For making TiO_2 -nf, $r = 5.5$; but for making TiO_2 -ns, $r = 3.5$.

The as-prepared xerogels (containing acetate ligands) were calcined at 673, 773, 873, 973, 1073, and 1173 K for two hrs with heating and cooling ramps of 5.0 K/min.

The as-prepared TiO_2 materials were labeled with a suffix ‘-353 K’, e.g., La(III)/ TiO_2 -dop-353 K. After calcination at a temperature ranging from 673 to 1173 K, the samples were labeled with a suffix -calcine temperature in Kelvin, e.g., La(III)/ TiO_2 -dop-773 K.

Synthesis of nanofibrous La(III) deposited TiO_2 (La(III)/ TiO_2 -dep). 11.37 g of $\text{La}(\text{NO}_3)_3(\text{H}_2\text{O})_6$ was dissolved in 50 g of deionized water, and into this solution was added 100 g of TiO_2 -nf-673 K under stirring. The resulting paste was covered with a glass lid and kept in an oven at 333 K for 2 h. After drying under vacuum at $T = 353$ K for 12 h, this material was calcined at temperatures range from 673 to 1173 K.

2.3. Claus reaction test

Even though the synthesized materials were calcined at different temperatures for studying their thermal stability, the catalyst testing was conducted only on the materials calcined at 773 K for two hrs, which was hot enough for crystallization of TiO_2 (anatase) while avoiding mesopore collapse under even higher temperatures.

Fig. 1 shows the experimental setup for the catalytic tests. 30.0% H_2O was supplied by a Waters 515 HPLC pump and vaporized by passing through a hot zone (450 K). The feed gas streams are supplied using mass flow controllers at typical industrial conditions for the first Claus converter, 8.15% H_2S , 3.94% SO_2 , 0.10% CS_2 , 0.10% COS and 57.71% N_2 [21]. The total flow rate was 445.6 mL/min, which provides a typical space velocity of 1200 h^{-1} . A pressure gauge, a relief valve and a bypass valve were used for safety purposes. An 2.1 cm i.d. stainless-steel reactor with six thermocouples was housed vertically in a resistively heated fluidized sand bed to achieve a uniform reaction temperature. 22.6 mL catalyst with a particle-size range of 3–4 mm was held by a stainless steel mesh in the reactor. The gas stream leaving the reactor was routed to a sulfur trap to collect liquid elemental sulfur (420 K), and KOH scrubbers were used to remove H_2S and SO_2 before the final effluent gas was emitted into the building plenum. In order to achieve a steady-state catalytic performance, all of the catalysts were calcined at 773 K and aged with 30% H_2O for 8 h, followed by exposure

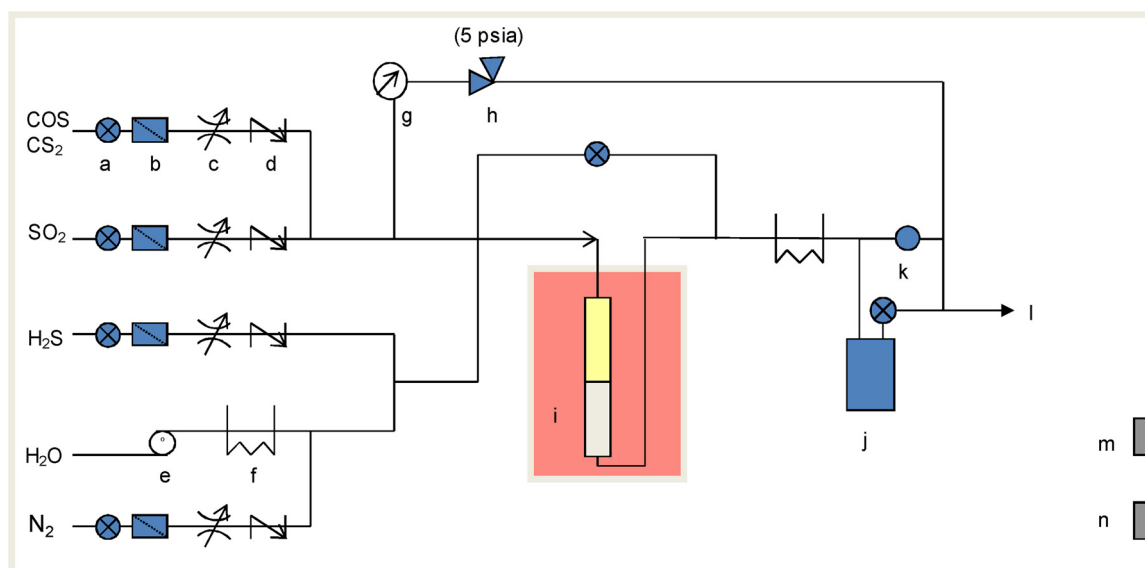


Fig. 1. Experiment setup for the Claus catalytic converter. (a) needle valves, (b) 5 μm stainless steel filters, (c) mass flow controllers, (d) check valves, (e) a water pump, (f) heating ropes, (g) pressure gauge, (h) relief valve, (i) furnace and reactor, (j) sulfur trap, (k) sample valve, (l) KOH trap and vent, (m) H_2S sensor, and (n) SO_2 sensor.

to a steam containing 8.15% H_2S and 3.94% SO_2 at 593 K for 8 h prior to the catalytic tests (pre-thermal aging and initial sulfation, following an industrial protocol) [21]. The Claus reaction temperature was varied from 543 to 593 K and a space velocity of 1200 h^{-1} (on the basis of the catalyst bed volume of 22.6 mL and a temperature of 293 K) was used for all of these tests. It is noted that 593 K and 543 K are used for first and second converter, respectively. Conversions of H_2S , CS_2 and COS were calculated from the gas chromatographic data. The sampling region was maintained at 473 K to avoid condensation of water. The gas samples were withdrawn right after the reactor into a syringe through P_2O_5 to remove water and avoid extraneous aquaClaus in the GC column. The dried gas samples were then analyzed by gas chromatography using a thermal conductivity detector (TCD) on a Varian CP-3800 GC. After each test, the reactor was flushed with N_2 and cooled down to room temperature.

In order to estimate the amount of elemental sulfur trapped in the catalyst, a quench procedure was performed on the reactor after the Claus reaction equilibrium was achieved at 543 K. The reactor bypass valve was opened immediately followed by closing all feed gas valves and natural cooling of the reactor. This process was designed to allow all of the elemental sulfur trapped in the catalyst bed to remain within the catalyst. After the reactor was cooled to room temperature, a N_2 flush was used to purge the remaining gas mixture containing H_2S and SO_2 into the KOH trap. The obtained catalysts were analyzed for elemental sulfur content by using a thermogravimetric analysis.

2.4. Catalyst characterization

A series of characterizations were carried out in order to understand the physical and chemical properties of the synthesized materials. Electrospray ionization mass-spectrometry (ESI-MS) analysis of the sol-gel liquid mixture was conducted on a Bruker Esquire 3000. Transmission electron microscopy (TEM) images were obtained using a Phillips Tecnai F20 operated at 200 kV. Scanning electron microscopy (SEM) images were recorded using a FEI Philips XL30 at 20 kV with prior gold coating to prevent specimen charging. The N_2 isotherms, BET surface areas and mesopore size distributions of the catalysts were determined by N_2 adsorption at 77 K on a 3Flex Surface Characterization Analyzer (Micromeritics). Elemental analysis was performed on an X-ray photoelectron spectrometer (XPS) (Axis Ultra, Kratos Analytical) and XRD data was obtained using a Rigaku Multiflex

diffractometer with a copper target at a speed of $2^\circ/\text{min}$ and a step size of 0.02° . Thermal gravimetric analysis (TGA) was conducted on a TA TGA 55 system. The samples were heated from $T = 298\text{--}873\text{ K}$ at a scanning rate of $\delta T = 10\text{ K min}^{-1}$ and the instrument was swept with 99.999% helium at a rate of 25 mL min^{-1} . Ionic chromatography (IC) samples were prepared using 0.10 N NaOH to extract sulfate and sulfite from the spent catalysts using sonication. All the processes were conducted under an inert environment in a N_2 glove bag to prevent oxidation of sulfur compounds by air. GC analysis was conducted on a Varian CP-3800 equipped with two columns (a molsieve 5 A and a Restek RT-U-Bond Plot) and two TCD detectors.

3. Results and discussion

3.1. CS_2 conversion tests

In the catalytic stage, H_2S conversion is a function of temperature and the reaction between H_2S and SO_2 (eq. 3) reaches thermodynamic equilibrium. In contrast, even though thermodynamic calculations show that CS_2 can be destructed completely at temperatures of 543 to 593 K, in reality it is very difficult to achieve catalytically. Hence, destruction of CS_2 is often used as an activity benchmark for the health of Claus catalysts. The catalyst performances can be compared from Fig. 2. First of all, all the TiO_2 catalysts achieved high CS_2 and COS conversions at 593 K. When the reaction temperature was dropped to 543 K, COS conversion remained relatively high for most of the catalysts; however, the CS_2 conversions were quite different and followed a trend of $\text{La(III)/TiO}_2\text{-dop} > \text{TiO}_2\text{-ns} \sim \text{TiO}_2\text{-nf} > \text{La(III)/TiO}_2\text{-dep}$. $\text{La(III)/TiO}_2\text{-dop}$ stood out for its 91.4% CS_2 conversion, an appealing number for the first catalytic converter.

With a lower reaction temperature, the ageing of the catalyst would be reduced and less heat would be required to achieve the inlet temperature (streams must be reheated due to upstream sulfur condensers). We note that the total Claus sulfur recovery is increased from 68.8% to 82.2% through lowering the catalytic temperature from 593 K to 543 K, thus the major benefit could be the reduction in temperature for the catalytic stages. In addition, the nanofibrous xerogels exhibit a very low bulk density. For instance, the density of $\text{La(III)/TiO}_2\text{-dop}$ is only 0.22 kg/L, about 76% lower than that of the conventional catalysts. Because the catalysts are compared with the same space velocity, or same volume of catalyst bed, a lower density means that less catalyst is

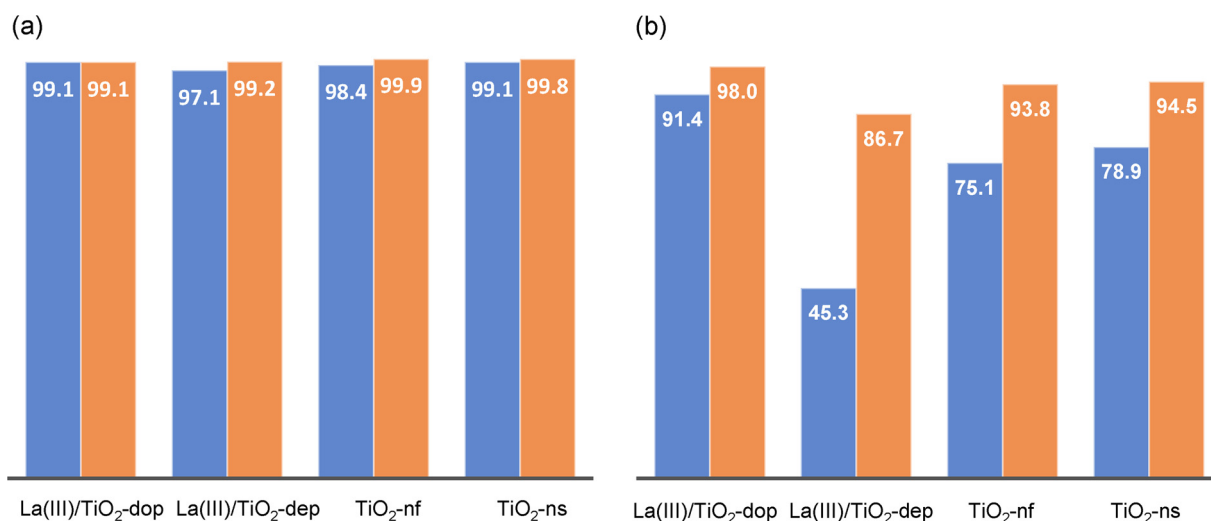


Fig. 2. CS₂ (blue) and COS (orange) conversions at a reaction time of 8 h by using different catalysts: (a) at 593 K, and (b) at 543 K. Feed concentrations: 0.10% CS₂, 0.10% COS, 8.15% H₂S, 3.94% SO₂, 29.95% H₂O, balanced with N₂; Space velocity = 1200 h⁻¹. (For interpretation of the references to colour in this figure legend, the reader is referred to the web version of this article.)

required for the conversions.

Note that the catalytic activities in Fig. 2 were compared to conversion after a reaction time of 8 hs. Compared to the CS₂/COS conversions at the initial stages, the nanofibrous La-modified catalysts (including La(III)/TiO₂-dop and La(III)/TiO₂-dep) showed no sign of CS₂ conversion change, indicating a high stability of the catalysts within 8 hs. On the other hand, the CS₂ conversion by using TiO₂-nf dropped from 81.3% to 75.1% at 543 K, which is attributed to the lower thermal stability of unmodified TiO₂ as described in the N₂ physisorption section. In addition, the CS₂ conversion by using TiO₂-ns dropped from 82.7% to 78.9% at 543 K, which is attributed to the liquid sulfur fouling within the small pores (see TGA section for more details).

In order to understand the CS₂ conversion trend, it is necessary to study the physical properties of the catalysts and the chemistry of the process. Herein, the morphology of the fibrous materials will be discussed first.

3.2. Electron microscopy

The visual appearance of nanofibrous TiO₂ xerogel shows no differences from the conventional TiO₂ that are comprised of spherical particles. Different from many reported nanofibers that are isolated nanoparticles [22], the nanofibers within a xerogel are linked with one another by chemical bonds and thus form a network. If this network is larger than millimetre size, it is called a monolith [23]. In fact, the xerogels produced in this study are in the form of one single piece and take the shape of the flask reactor. After breaking down the monolith and grinding, the resulting particulates have a size range from tens to hundreds of micrometers (Fig. 3a), similar to the powder of conventional catalysts and zeolites, which are used for making catalyst or

adsorbent pellets for industries [24]. In contrast to the very dense packed spherical particles (mostly crystallites) of the conventional TiO₂, the nanofibrous TiO₂ shows plenty of empty spaces between the fibers (Fig. 3b and c), and these spaces contribute to the overall macroporosity (> 50 nm). In the conventional TiO₂, the void space between the close packed TiO₂ crystallites is the origin of the mesopores (2–50 nm) [25]. In order to introduce macropores, catalyst producers can add hydrocarbons into the metal oxide powder paste before making pellets, followed by calcination to burn out the hydrocarbons. However, these deliberately added macropores are not comparable to that of nanofibrous xerogel, evidenced by their very low density not seen for the conventional catalysts (Table 1).

More structure details within the nanofibers are revealed in Fig. 4. The diameters of the nanofibers are ca. 30 nm (Fig. 4a). At a higher resolution, the dark spots with sharp edges in Fig. 4b show the presence of crystallites in the size range of 11–16 nm. Inside a nanofiber, the little white areas between the crystallites show the existence of mesopores and their sizes are within a few nanometers. It is noted that the exterior surface of the nanofibers in Fig. 4a and b is in fact the interior surface of macropores within a nanofibrous network. The surface within both mesopores and macropores provides active sites for chemisorption and catalytic activity. The high-resolution TEM images (Fig. 4c) exhibit the signature 0.35 nm lattice spacing of (101) planes and the 0.24 nm lattice spacing of (004) planes that belong to the anatase phase.

3.3. N₂ physisorption

BET surface area, pore size and pore volumes of catalyst candidates are important parameters for determination of their performance. All of the nanofibrous and spherical materials in Fig. 5a show Type IV

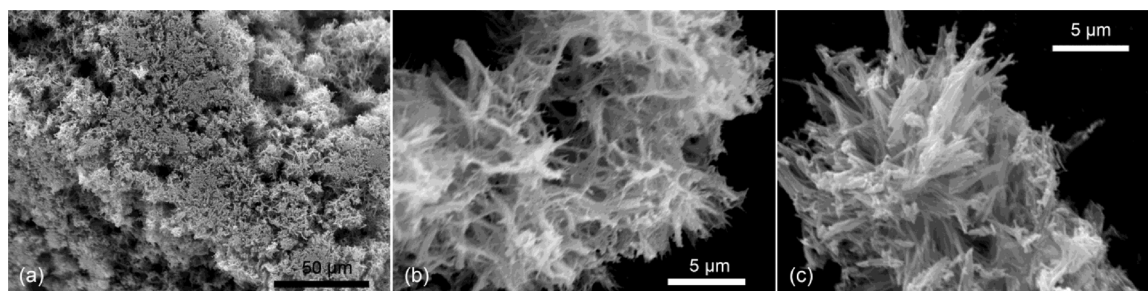


Fig. 3. SEM images of La(III)/TiO₂-dop-773 K (a and b), and La(III)/TiO₂-dep-773 (c).

Table 1
Catalyst bulk densities.

Samples	La(III)/TiO ₂ -dop	La(III)/TiO ₂ -dep	TiO ₂ -nf	TiO ₂ -ns
$d_{\text{bulk}}/\text{kg L}^{-1}$	0.22	0.24	0.20	0.92

isotherms, which is typical for metal oxide materials with mesopores. However, the slopes of the fibrous materials after $p/p^\circ > 0.5$ indicate the existence of a wide range of pore sizes. The H3 hysteresis loops belonging to the fibrous materials indicate slit-like pore structures, possibly contributed by the void space between the parallel nanofibers as shown in Fig. 3a. On the other hand, the H2 hysteresis loop of the spherical materials suggests mesopores with possible interconnecting channels between the pores, which results from the void space between the spherical crystallites being partially fused together during the calcination process. In Fig. 5b, the pore size profiles of La(III)/TiO₂-dop-773 K and TiO₂-ns-673 K are compared. Apparently, the nanofibrous structure exhibited a larger pore size and a wider pore size distribution, which agrees with the observation under the electron microscope. It is noted that during the N₂ isotherm measurement, small pores are filled with liquid nitrogen first due to the capillary condensation effect. With an increased N₂ vapor pressure, larger pores will then be filled. When the pressure reaches p° , all the macropores are theoretically filled with liquid nitrogen at equilibrium. It is not easy to measure the macropores using liquid nitrogen because the pore filling occurs at pressures too close to the vapor pressure [26]. This pore filling phenomenon can be used to explain the sulfur condensation behavior within the Claus catalyst bed, because the sulfur vapor pressure for lower temperature catalytic converters (543 K) is not far from the dew point temperature (517 K).

In Table 2, the BET surface area, pore sizes and pore volumes of the fibrous and spherical materials are listed. First of all, the nanofibrous materials show a higher surface area, pore size and pore volume than the spherical catalyst, and this difference is more pronounced after higher temperature calcination. This is in line with the microstructure differences as disclosed in the electron microscopy section. Different from the close packed spherical particles that tend to fuse together at an elevated temperature [27], the nanofibers are far away from one another and therefore they are more difficult to combine together. As a consequence, the surface areas and pore structures of the nanofibrous materials are less affected by the sintering. Secondly, addition of La(III) also helps to maintain a high surface area after a high temperature treatment. It is noted that a stabilized microstructure is very important for a catalyst that is used in high temperature reactions, especially with the presence of H₂O and fouling substances. Thirdly, the thermal stability of La(III) doped TiO₂ is very similar to that of La(III) deposited TiO₂.

After the Claus reaction tests operated at no more than 593 K, the BET surface area of TiO₂-ns-673 K dropped from 74 to 40 m² g^{−1}. It should be mentioned that TiO₂-ns-673 K had experienced calcination at 673 K for 2 h prior to the catalytic tests. This pronounced surface area loss is attributed to the high concentration of water vapor, which causes small pore shrinkage [28]. In contrast, the surface area of La(III)/TiO₂-dop-773 K after the Claus reactions decreased insignificantly from 102 to 98 m² g^{−1}. This further indicates that the La(III)-doping improved the thermal stability (maybe chemical stability as well) of the materials.

The thermal stabilization effect of La(III) on TiO₂ can also be observed from powder XRD. As mentioned previously, the mesopores of metal oxides are attributed to the void space between the crystallites. If the crystallites are sintered upon heating, the mesopores will shrink and may eventually disappear. In Table 3, the anatase and rutile crystallite sizes and their ratios are compared. In all of these samples, the small anatase crystallites grow into a larger size upon heat treatment. In addition, a phase change from anatase to rutile can also be observed for all TiO₂. However, both crystalline phase transition and crystallite size increments followed a trend of La(III)/TiO₂-dop < La(III)/TiO₂-dep < TiO₂-nf < TiO₂-ns, because of the crystalline changes needed to overcome the barriers of La(III) dopant and void space as discussed earlier.

3.4. Thermogravimetric analysis (TGA)

A thermogravimetric analysis was conducted on the spent catalyst samples obtained from the quenched reactor (see experimental section). Fig. 6a shows the weight loss profiles of the spent La(III)/TiO₂-dop-773 K and TiO₂-ns-673 K in the temperature range of 308–873 K. The weight loss in the range of 298–405 K is assigned to the physisorbed water, and the loss in the range of 405–531 K is attributed to the elemental sulfur trapped in the mesopores. The sulfur trapped in the nanospherical catalyst is as high as 6.6 wt.%; in contrast, only 2.06 wt.% sulfur is trapped in the nanofibrous catalyst. Taking account of the lower density of nanofibrous catalyst (24% of nanospherical TiO₂), there is significantly less total sulfur in the nanofibrous catalyst bed. Because more sulfur is trapped in TiO₂-ns-673 K, which has a smaller surface area (74 m² g^{−1}), in comparison to the La(III)/TiO₂-dop-773 K (102 m² g^{−1}) (see Table 2), the adsorbed elemental sulfur is not related to the surface area, but to the pore size. As is the case for any adsorbate near its dew point temperature, the elemental sulfur filled up the smallest pores first. On the basis of accumulated pore volume as a function of pore size (Fig. 6b) and the amount of sulfur trapped in the catalysts, the critical pore sizes for sulfur condensation at 543 K are determined to be 3.13 nm (TiO₂-ns) and 3.05 nm (La(III)/TiO₂-dop) (see Fig. 6b inset).

The Kelvin equation is often used to estimate pore size distribution

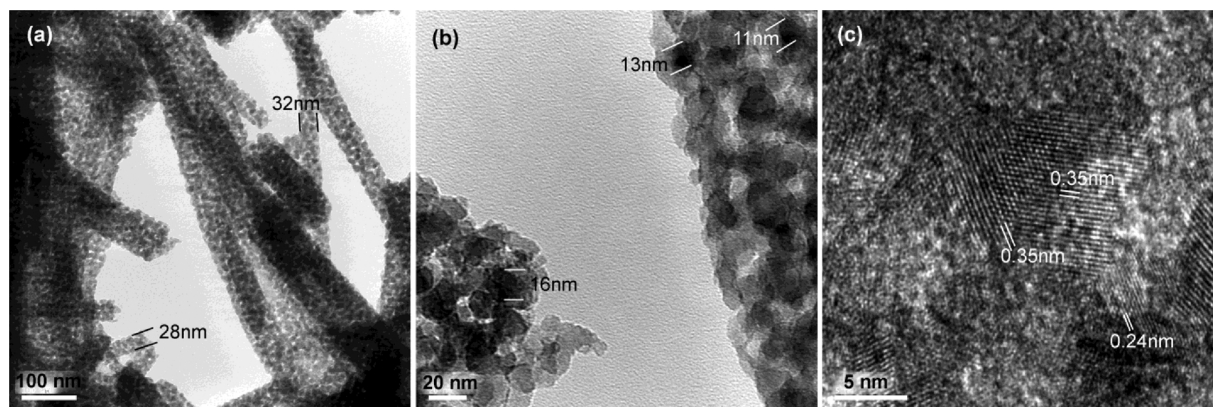


Fig. 4. TEM images of La(III)/TiO₂-dop-773 K with increased magnification from left to right. (a) nanofibers with diameters ca. 30 nm; (b) the nanofibers are composed of nanocrystallites less than 16 nm; (c) the signature anatase lattice fringe patterns.

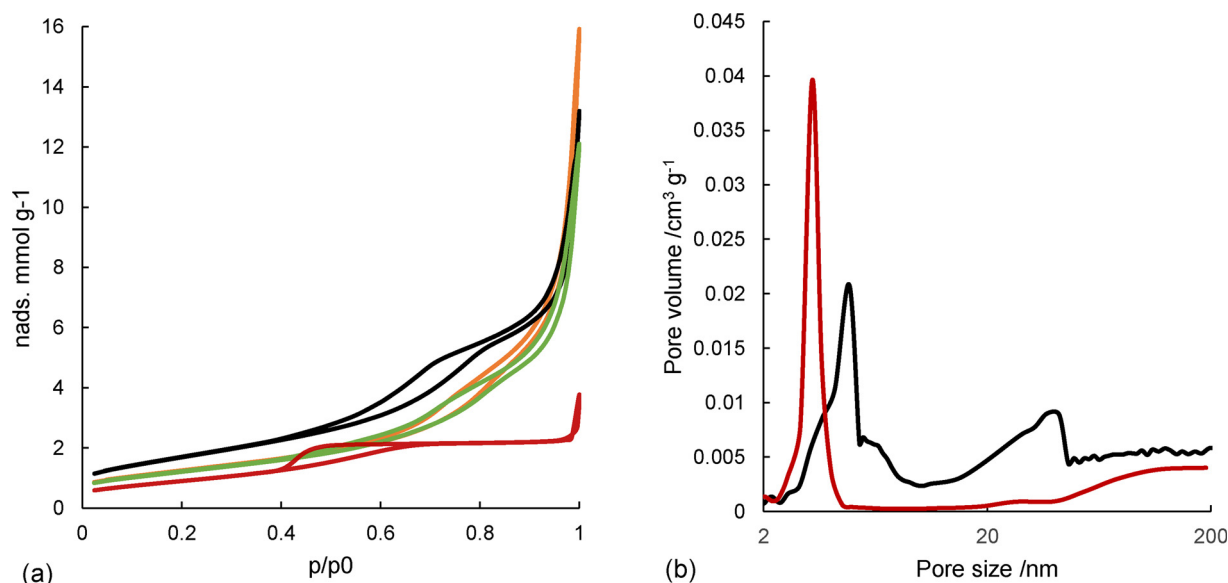


Fig. 5. (a) Isotherms of La(III)/TiO₂-dop-773 K (black), La(III)/TiO₂-dep-773 K (orange), TiO₂-nf-773 K (green), and TiO₂-ns-673 K (red); (b) JBH desorption pore size distribution of La(III)/TiO₂-dop-773 K (black) and TiO₂-ns-673 K (red). (For interpretation of the references to colour in this figure legend, the reader is referred to the web version of this article.)

Table 2

The specific BET surface area, pore size and pore volume of La₂O₃/TiO₂, TiO₂ nanofibers and nanospheres calcined at 673–1173 K.

Sample	BET (m ² /g)	Pore size ^a (nm)	Pore volume ^b (cm ³ /g)
La(III)/TiO ₂ -dop-353 K	256	5.4	0.35
La(III)/TiO ₂ -dop-673 K	138	11.6	0.40
La(III)/TiO ₂ -dop-773 K	102	13.4	0.34
La(III)/TiO ₂ -dop-873 K	73	18.8	0.35
La(III)/TiO ₂ -dop-973 K	42	22.4	0.24
La(III)/TiO ₂ -dop-1073 K	22	23.7	0.13
La(III)/TiO ₂ -dop-1173 K	14	22.8	0.08
La(III)/TiO ₂ -dep-673 K	100	20.2	0.50
La(III)/TiO ₂ -dep-773 K	89	17.0	0.38
La(III)/TiO ₂ -dep-873 K	74	22.5	0.41
La(III)/TiO ₂ -dep-973 K	52	25.9	0.33
La(III)/TiO ₂ -dep-1073 K	35	32.1	0.28
La(III)/TiO ₂ -dep-1173 K	15	22.8	0.08
TiO ₂ -nf-353 K	234	6.0	0.35
TiO ₂ -nf-673 K	98	15.3	0.37
TiO ₂ -nf-773 K	53	20.3	0.27
TiO ₂ -nf-873 K	50	25.4	0.31
TiO ₂ -nf-973 K	20	26.5	0.14
TiO ₂ -nf-1073 K	11	32.9	0.09
TiO ₂ -nf-1173 K	3	8.6	0.007
TiO ₂ -ns-353 K	311	2.8	0.22
TiO ₂ -ns-673 K	74	4.9	0.09
TiO ₂ -ns-773 K	15	9.7	0.06
TiO ₂ -ns-873 K	1	66.2	0.02
TiO ₂ -ns-973 K	1	45	0.02
TiO ₂ -ns-1073 K	1	36	0.01
TiO ₂ -ns-1173 K	1	100	0.02

Catalyst testing was performed only for '773 K' samples.

of porous materials (eq. 6) [26]. Fig. 7 shows the sulfur vapor pressures as a function of the size of pores that are filled with liquid sulfur, estimated by using Kelvin equation. Using the calculated sulfur vapor concentration in the reactor at 543 K, 0.757%, the critical pore size is estimated to be 4.29 nm. Given the fact that the surface property of the catalyst and/or changing adsorbate vapor composition are not considered in Kelvin equation, the discrepancy between the experimental (3.13 nm) and theoretical value (4.29 nm) is acceptable. It is noted that these values are also comparable to the results reported by others [29]. Because of condensation of liquid sulfur in the small pores, the pore

Table 3

Anatase (101) position and the Scherrer crystallite size.

Samples	2-theta (°)	D _{Scher} ^a (nm)	ana./rut. ^b
La(III)/TiO ₂ -dop-673 K	25.7	7	1/0
La(III)/TiO ₂ -dop-773 K	25.7	11	1/0
La(III)/TiO ₂ -dop-873 K	25.8	13	1/0
La(III)/TiO ₂ -dop-973 K	25.7	15 (19) [†]	0.81/0.19
La(III)/TiO ₂ -dop-1073 K	25.6	19 (20) [†]	0.60/0.20
La(III)/TiO ₂ -dop-1173 K	25.7	20 (27) [†]	0.19/0.81
La(III)/TiO ₂ -dep-673 K	25.7	14	1/0
La(III)/TiO ₂ -dep-773 K	25.7	14	1/0
La(III)/TiO ₂ -dep-873 K	25.6	15	1/0
La(III)/TiO ₂ -dep-973 K	25.7	15	0.89/0.11
La(III)/TiO ₂ -dep-1073 K	25.7	18(19) [†]	0.82/0.18
La(III)/TiO ₂ -dep-1173 K	25.7	23(24) [†]	0.34/0.66
TiO ₂ -nf-673 K	25.3	13	1/0
TiO ₂ -nf-773 K	25.4	16	1/0
TiO ₂ -nf-873 K	25.3	16	0.71/0.29
TiO ₂ -nf-973 K	25.3	31	0.49/0.51
TiO ₂ -nf-1073 K	–	(26) [†]	0.15/0.85
TiO ₂ -nf-1173 K	–	(29)	0.03/0.97
TiO ₂ -ns-673 K	25.3	10	1/0
TiO ₂ -ns-773 K	25.3	13	0.88/0.12
TiO ₂ -ns-873 K	25.3	29(29) [†]	0.11/0.89
TiO ₂ -ns-973 K	–	(34) [†]	0/1
TiO ₂ -ns-1073 K	–	(34) [†]	0/1
TiO ₂ -ns-1173 K	–	(41) [†]	0/1

Note: ^a The crystallite size estimated using Scherrer's equation and powder XRD data; ^b anatase/rutile molar ratio; [†] the number in the bracket shows the crystallite sizes of rutile crystallites; catalyst testing was performed only for '773 K' samples.

sizes of a catalyst play a more important role than surface area. This conclusion is also supported by the test results of a commercial TiO₂ catalyst, which shows a BET surface area of 140 m² g⁻¹ but similar pore structure. The CS₂ conversions between this catalyst and TiO₂-ns are very similar, even though the latter has a low surface area of 74 m² g⁻¹.

$$\ln \frac{p}{p^0} = \frac{2\gamma V_m}{rRT} \quad (6)$$

Where p and p^0 are the vapor pressure and saturated vapor pressure, respectively, γ is the surface tension, V_m is the molar volume of the liquid, R is the universal gas constant, r is the radius of the droplet/pore

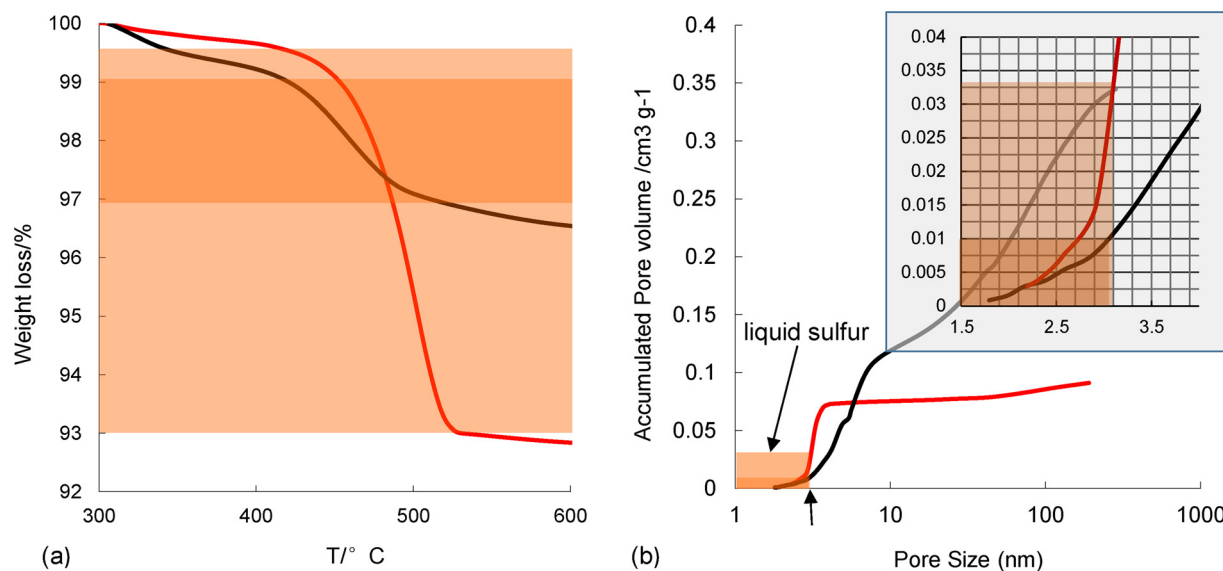


Fig. 6. (a) TGA results of spent La(III)/TiO₂-dop-773 K (black) and TiO₂-ns-673 K (red) in the temperature range of 308–873 K; (b) accumulated pore volumes with increased pore sizes of spent La(III)/TiO₂-dop-773 K (black) and TiO₂-ns-673 K (red), the inset shows the critical pore sizes for liquid sulfur fouling. (For interpretation of the references to colour in this figure legend, the reader is referred to the web version of this article.)

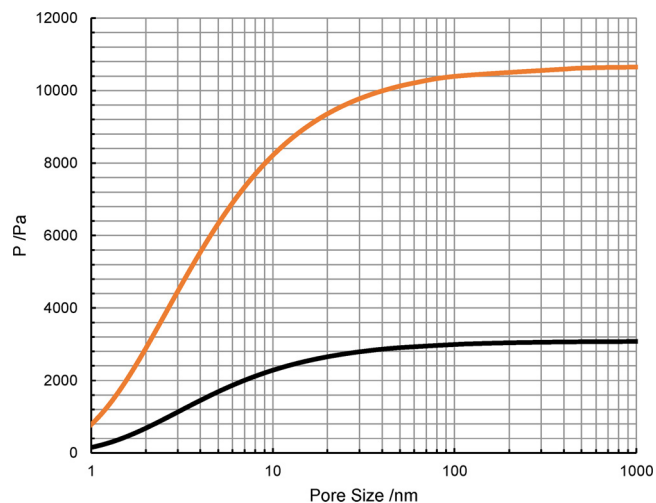


Fig. 7. Equilibrium sulfur vapor pressure vs. pore (filled with liquid sulfur) radius at 543 (black) and 593 K (orange), estimated by using Kelvin equation. The sulfur surface tensions are 0.0502 and 0.0475 N m⁻¹ at 543 K and 593 K, respectively [30]; the sulfur vapor pressures are 3085.9 and 10,665.8 Pa at 543 K and 593 K, respectively [31].

size, and T is temperature.

It should be noted that 30% water vapor is also present during the tests, but water condensation in the catalysts can be ignored. Using the Kelvin equation, the critical radii of cylindrical pores for water condensation was calculated to be 0.34 nm, and the portion of surface area below this pore size is very small [6]. Therefore, the condensed water is not expected to affect the catalytic performance.

According to Table 1, clearly La(III) has a significant effect on TiO₂ catalytic performance. While La(III) doping significantly improves CS₂ conversion, La(III) deposition has the opposite effect. Thus, it is important to understand the difference between these materials. Differing from deposition methods that often result in foreign domains on the surface of a support, the co-sol-gel processing of the lanthanum and titanium organic precursors is expected to generate a more uniform distribution of mixed oxides.

3.5. Mass spectrometry

ESI-MS is able to reveal the intermediates of metal-ligand complexes during reactions. Our previous reports have shown the mass-spectra of Ti-oxo-acetates by analyzing the mixture of Ti(OⁱPr)₄ and acetic acid at the initial stage of sol-gel reaction [15]. In order to introduce La(III) into the Ti complexes, a soluble La(OAc)₃ precursor was selected. As Ti(OⁱPr)₄ is known to react quickly with acetic acid [32], it is essential to dissolve La(OAc)₃ first in the acetic acid-heptane solution, followed by addition of Ti(OⁱPr)₄ under stirring. Fig. 8 shows the mass-spectra of the reaction mixture of La(OAc)₃, acetic acid, and Ti(OⁱPr)₄, after ca. 5 min of mixing at 333 K. The assignments of these peaks (Table 4) clearly show that La(III) was incorporated in the metal-oxo-acetate complexes. It is anticipated that La(III) would remain in the TiO₂ matrix upon calcination, which is important for its catalytic activity.

3.6. X-ray photoelectron spectroscopy

Because the sulfur compounds (H₂S, SO₂, CS₂ and COS) to be converted in the Claus reactions are acidic, it is rational to seek basic active sites responsible for their adsorption. The oxygen defects including oxygen vacancy and hydroxide of TiO₂ can be detected by XPS (Fig. 9 and Table 5) [33,34]. Both La(III)/TiO₂-dop-773 K and La(III)/TiO₂-dep-773 K show a higher oxygen vacancy and –OH concentrations than TiO₂-nf; however, there is not much difference between the two La(III) modified samples. The –OH is believed to be responsible for CS₂ destruction as described in the discussion section. Under Claus reaction conditions, it is anticipated that H₂O may take the oxygen vacancy because the vapor concentration was as high as 30%. It is noted that O₂ is absent, but SO₂ might compete with H₂O for the active sites.

3.7. Sulfate contents

Sulfate was detected in the spent catalysts by both IC and XPS analysis. IC results in Table 6 shows that there was less sulfate formation when La(III) was present. At this point it is not clear if oxygen defects reduce sulfate formation. Previous reports by both Huang and Lavalley et al. have shown that sulfate affected CS₂ conversion [35–37], which agree with our observation: TiO₂-ns shows a higher concentration of sulfate and low CS₂ conversion. At the same time, sulfate is an intermediate in the Claus reaction; therefore, sulfate must be present to

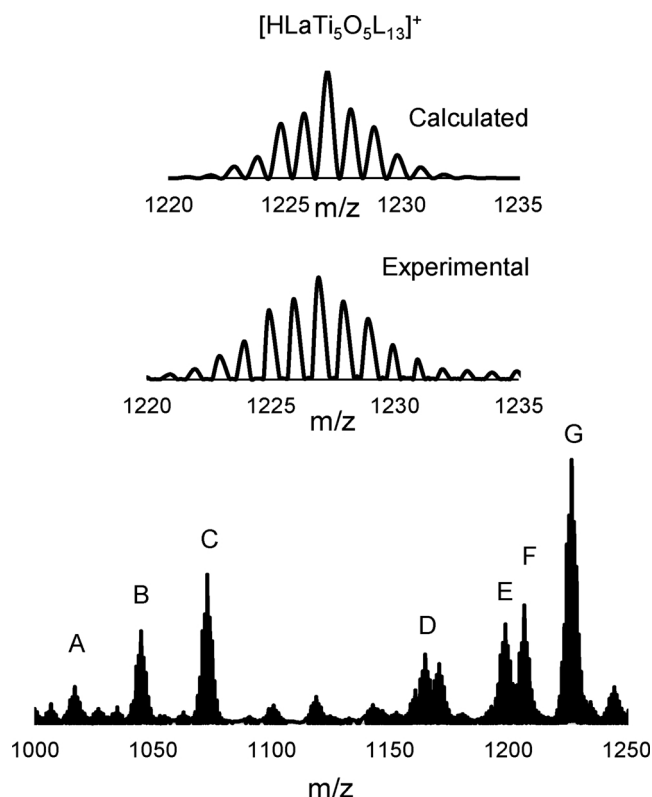


Fig. 8. Electrospray experimental and calculated mass-spectra of $\text{Ti}(\text{O}^i\text{Pr})_4$ and $\text{La}(\text{OAc})_3$ in heptane after reaction with 5.5 mol equiv of acetic acid at 333 K. Selected m/z signal assignments are listed in Table 4.

Table 4

Proposed molecular fragments corresponding to the mass spectra in Fig. 8. L = $-\text{OAc}$ or $-\text{O}^i\text{Pr}$.

Fragment	Assignment	Exp.	Calc.
A	$[\text{La}_2\text{Ti}_3\text{O}_4\text{L}_9]^+$	1017.0	1017.1
B	$[\text{HLaTi}_4\text{O}_4\text{L}_{11}]^+$	1045.0	1045.2
C	$[\text{HTi}_5\text{O}_3\text{L}_{13}(\text{OH})]^+$	1073.0	1073.3
D	$[\text{HLaTi}_4\text{O}_2\text{L}_{13}(\text{OH})_2]^+$	1165.0	1165.4
E	$[\text{La}_2\text{Ti}_4\text{O}_5\text{L}_{11}]^+$	1198.9	1199.1
F	$[\text{HTi}_4\text{O}_2\text{L}_{14}(\text{OH})]^+$	1206.9	1207.3
G	$[\text{HLaTi}_5\text{O}_5\text{L}_{13}]^+$	1226.9	1227.3

some extent. On the basis of our IC results, while $\text{La}(\text{III})/\text{TiO}_2$ -dop and $\text{La}(\text{III})/\text{TiO}_2$ -dep have similar sulfate concentrations, their catalytic activity for CS_2 are quite different and we know there are other factors that affected the CS_2 reaction. XPS did not detect either thiosulfate or

Table 5

The lattice oxygen, $-\text{OH}$, and oxygen vacancy provided by XPS O_{1s} .

	$\text{O}_{1s,\text{latt.}}^a$		$\text{O}_{1s,\text{OH}}^b$		$\text{O}_{1s,\text{vac.}}^c$	
	conc. % ^d	fwHM ^e	conc. %	fwHM	conc. %	fwHM
$\text{La}(\text{III})/\text{TiO}_2$ -dop	85.55	1.06	8.07	1.03	6.38	1.03
$\text{La}(\text{III})/\text{TiO}_2$ -dep	84.0	1.05	7.90	1.03	8.10	1.03
TiO_2 -nf	88.16	1.06	4.50	1.03	7.34	1.03

Note: ^a lattice oxygen; ^b hydroxide; ^c oxygen vacancy; ^d concentration; and ^e full width at half maximum.

Table 6

Sulfate, sulfite and thiosulfate concentrations of the spent catalysts.

Sample	$\text{La}(\text{III})/\text{TiO}_2$ -dop	$\text{La}(\text{III})/\text{TiO}_2$ -dep	TiO_2 -ns
SO_4^{2-} (wt.%)	1.26	1.25	4.41
SO_3^{2-} (wt.%)	0.24	0.13	0.10
$\text{S}_2\text{O}_3^{2-}$ (wt.%)	0.01	0.11	0.02

sulfur (Fig. 10), possibly because their concentrations were too low. It is noted that these samples for XPS analysis were flushed with N_2 at a high temperature to remove sulfur compounds.

4. Discussion

Both $\text{La}(\text{III})$ -doped and $\text{La}(\text{III})$ -deposited TiO_2 shows very high thermal stability, but their activity for CS_2 conversions are surprisingly different. While $\text{La}(\text{III})$ -doped TiO_2 exhibits the highest catalytic activity, the $\text{La}(\text{III})$ -deposited counterpart is worse than pure TiO_2 . We propose that this phenomenon is related to the structure discrepancy between the two catalysts and coverage of active sites; furthermore, it sheds light on the CS_2 destruction mechanism.

XPS results demonstrated that concentrations of $\text{La}(\text{III})$ in $\text{La}(\text{III})$ -doped and -deposited samples were 0.47 and 0.79% $\text{La}(\text{III})/\text{TiO}_2$, respectively, even though their molar ratios of La/Ti were targeted to be the same (2.5%). The richer $\text{La}(\text{III})$ concentration in the deposited TiO_2 was due to the fact that XPS only examined the top few layers of the sample, and it is difficult for the deposited $\text{La}(\text{III})$ to penetrate into the TiO_2 matrix. In contrast, $\text{La}(\text{III})$ was readily mixed with TiO_2 by sol-gel doping, hence it was not surprising for lanthanum to be undetectable by powder XRD. Somewhat surprisingly, the powder XRD did not detect La_2O_3 or $\text{La}(\text{OH})_3$ peaks in the $\text{La}(\text{III})$ deposited sample either. However, the anatase (101) peak was shifted from ca. 25.38° to 25.75° 2θ after La -modification. In addition, the literature suggests that $\text{La}(\text{III})$ may be difficult to detect unless its concentration is very high. A tunneling electron microscopy study suggests that La_2O_3 forms a thin layer on the top of TiO_2 [38]. In addition, $\text{La}(\text{III})$ was reported to exist in a form of $\text{La}(\text{OH})_3$ [39], which agree with our XPS observation that shows

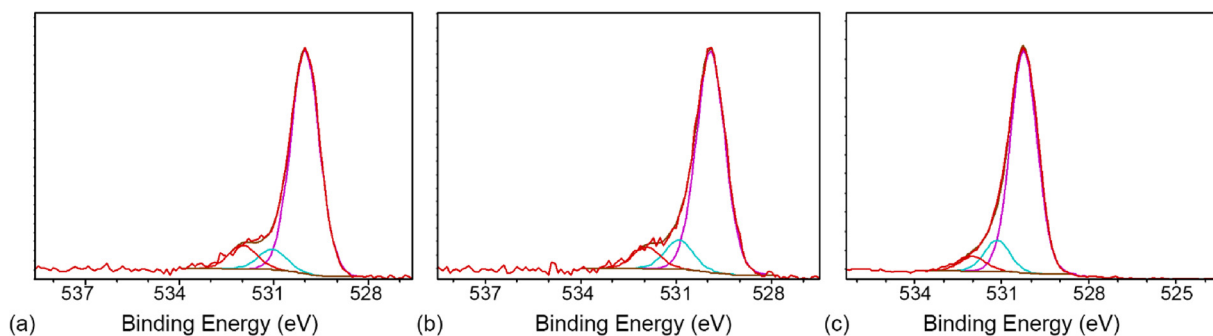


Fig. 9. O_{1s} of $\text{La}(\text{III})/\text{TiO}_2$ -dop-773 K nanofibers (a), $\text{La}(\text{III})/\text{TiO}_2$ -dep-773 K nanofibers (b), and TiO_2 nanofibers (c). The peaks at ca. 532 eV (red), 531 eV (blue) and 530 eV (pink) are assigned to oxygen $-\text{OH}$, oxygen vacancy and lattice oxygen, respectively. (For interpretation of the references to colour in this figure legend, the reader is referred to the web version of this article.)

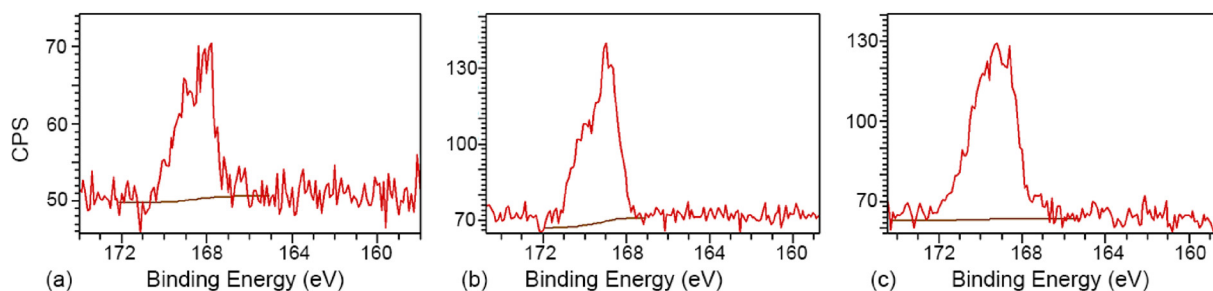


Fig. 10. XPS. High resolution scan of S_{2p} : (a) La(III)/TiO₂-dop, (b) La(III)/TiO₂-dep and (c) TiO₂-ns.

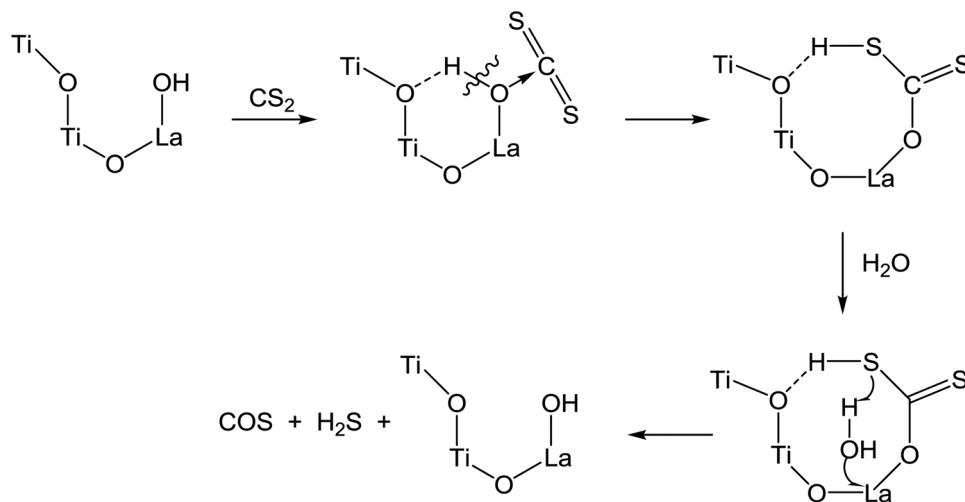


Fig. 11. Schematic drawing of the Lewis base-Lewis acid interaction of La–OH and CS₂, formation of intermediates, destruction of CS₂ and formation of H₂S and COS.

La(III) resulting in a high concentration of OH.

While the high activity of La(III)-doped TiO₂ suggests that more oxygen defects favors CS₂ conversion (Fig. 9), the low activity of La(III)-deposited TiO₂ indicated that a high coverage of La(III) on TiO₂ inhibits the reaction. Thus, a more controlled distribution of La(III) seems crucial for CS₂ destruction, similar to single atom Pt/CeO₂ for CO oxidation [40]. On the basis of the above discussion, we propose that both La–OH and TiO₂ domains are required in order to activate CS₂ molecules. Similar to the initial structure of COS on Al₂O₃ by quantum chemical calculations [41], CS₂ is chemisorbed to a hydroxide site following a Lewis acid-Lewis base interaction as shown in Fig. 11. The activated CS₂ would experience a sequence of intermediates, and COS and H₂S would be produced after the H₂O attack (Fig. 11). It should be mentioned that both a hydroxide and a neighboring bridging oxo bond is required for this mechanism.

As a more active molecule than CS₂, COS would readily react with SO₂ to form sulfur and CO₂ [35], or via a similar route as shown in Fig. 11 by interacting with –OH first, followed by producing CO₂ and H₂S.

5. Conclusion

The anisotropic self-assembly of bimetallic acetate complexes is a promising technique for synthesizing new catalysts that exhibit macropores and high catalytic activities towards CS₂ destruction because of their antifouling and tunable electronic properties. The nanofibrous xerogel has an advantage over conventional catalysts when high dew-point species such as liquid sulfur are present. This research demonstrates the potential of La-doped TiO₂ for Claus catalysts: not only can the reaction temperature be substantially decreased (increasing the thermodynamically limited Claus sulfur recovery), but also the amount

of catalyst is reduced due to its very low density. La(III) doping is found to introduce oxygen defects which promote catalytic activity, in addition to its ability for increasing the thermal stability of TiO₂. Also, a well-distributed Lewis-base was found to be essential for the CS₂ conversion reactions. Future work would be to optimize the catalytic performance by tuning the synthesis procedures and concentration of La (III) doping, and to use in-situ FTIR technique for studying CS₂/COS conversion mechanism.

Acknowledgements

This research has been funded through the Natural Science and Engineering Research Council of Canada (NSERC) and Alberta Sulphur Research Ltd. (ASRL) Industrial Research Chair program in Applied Sulfur Chemistry. The authors are grateful to NSERC and supporting member companies of ASRL. We thank Wade White, Tobias Furstenthaupt, and Michael Schoel of University of Calgary for their assistance on the mass-spec, powder XRD, TEM, and SEM characterizations. We also thank Drs. A. He and S. Xu of University of Alberta for XPS analysis.

References

- [1] A.B. Jensen, C. Webb, *Enzyme Microb. Technol.* 17 (1995) 2–10.
- [2] K.G. Wynnnyk, B. Hojjati, P. Pirzadeh, R.A. Marriott, *Adsorption* 23 (2017) 149–162.
- [3] S. Mortazavi-Manesh, A. Satyro Marco, A. Marriott Robert, *AIChE J.* 59 (2013) 2993–3005.
- [4] S. Eow John, *Environ. Prog.* 21 (2004) 143–162.
- [5] K. Karan, L.A. Behie, *Ind. Eng. Chem. Res.* 43 (2004) 3304–3313.
- [6] C. Rhodes, S.A. Riddell, J. West, B.P. Williams, G.J. Hutchings, *Catal. Today* 59 (2000) 443–464.
- [7] B. ZareNezhad, *J. Ind. Eng. Chem.* 15 (2009) 143–147.
- [8] R.L. Mora, *J. Hazard. Mater.* 79 (2000) 103–115.
- [9] X. Chen, A. Selloni, *Chem. Rev.* 114 (2014) 9281–9282.

- [10] U. Diebold, Surf. Sci. Rep. 48 (2003) 53–229.
- [11] C.P. Sibu, S.R. Kumar, P. Mukundan, K.G.K. Warriar, Chem. Mater. 14 (2002) 2876–2881.
- [12] A.-W. Xu, Y. Gao, H.-Q. Liu, J. Catal. 207 (2002) 151–157.
- [13] J. Zhang, Z. Zhao, X. Wang, T. Yu, J. Guan, Z. Yu, Z. Li, Z. Zou, J. Phys. Chem. C 114 (2010) 18396–18400.
- [14] T. Ohno, K. Sarukawa, K. Tokieda, M. Matsumura, J. Catal. 203 (2001) 82–86.
- [15] R. Sui, V. Thangadurai, C.P. Berlinguette, Chem. Mater. 20 (2008) 7022–7030.
- [16] R. Sui, J.M.H. Lo, C.B. Lavery, C.E. Deering, K.G. Wynnyk, N. Chou, R.A. Marriott, J. Phys. Chem. C 122 (2018) 5141–5150.
- [17] A. Lucky Rahima, A. Charpentier Paul, Adv. Mater. 20 (2008) 1755–1759.
- [18] P.D. Clark, R. Sui, Z. Premji, V. Thangadurai, S.S. Bhella, J. Sulfur Chem. 33 (2012) 131–142.
- [19] R. Sui, S.K. Carefoot, C.B. Lavery, C.E. Deering, K.L. Lesage, N. Chou, C.J. Rose, R.A. Marriott, J. Mater. Chem. A 5 (2017) 9561–9571.
- [20] H. Schaper, E.B.M. Doesburg, L.L. Van Reijen, Appl. Catal. 7 (1983) 211–220.
- [21] A. Kohl, R. Nielsen, Gas purification, fifth ed., Gulf Publishing Company, 1997 Houston.
- [22] M. Niederberger, Acc. Chem. Res. 40 (2007) 793–800.
- [23] C.J. Brinker, G.W. Scherer, Sol-Gel Science, Academic Press, San Diego, 1990 pp. xvi-18..
- [24] F. Akhtar, L. Andersson, S. Ogunwumi, N. Hedin, L. Bergström, J. Eur. Ceram. Soc. 34 (2014) 1643–1666.
- [25] R. Sui, A. Rizkalla, P.A. Charpentier, Microporous Mesoporous Mater. 142 (2011) 688–695.
- [26] J.B. Condon, Surface Area and Porosity Determinations by Physisorption, Elsevier Science, Amsterdam, 2006, pp. 1–27.
- [27] C.J. Brinker, G.W. Scherer, Sol-Gel Science, Academic Press, San Diego, 1990, pp. 674–742.
- [28] R. Sui, P. Charpentier, Chem. Rev. 112 (2012) 3057–3082.
- [29] S. Tong, I.G. Dalla Lana, K.T. Chuang, Can. J. Chem. Eng. 70 (2009) 516–522.
- [30] R. Fanelli, J. Am. Chem. Soc. 72 (1950) 4016–4018.
- [31] W.A. West, A.W.C. Menzies, J. Phys. Chem. 33 (1928) 1880–1892.
- [32] R. Sui, A.S. Rizkalla, P.A. Charpentier, Cryst. Growth Des. 8 (2008) 3024–3031.
- [33] J. Socratous, K.K. Banger, Y. Vaynzof, A. Sadhanala, A.D. Brown, A. Sepe, U. Steiner, H. Sirringhaus, Adv. Funct. Mater. 25 (2015) 1873–1885.
- [34] R. Schaub, P. Thstrup, N. Lopez, E. Lægsgaard, I. Stensgaard, J.K. Nørskov, F. Besenbacher, Phys. Rev. Lett. 87 (2001) 266104.
- [35] P.D. Clark, N.I. Dowling, M. Huang, Appl. Catal. B. 31 (2001) 107–112.
- [36] E. Laperdrix, A. Sahibed-dine, G. Costentin, O. Saur, M. Bensitel, C. Nédéz, A.B. Mohamed Saad, J.C. Lavalley, Appl. Catal. B. 26 (2000) 71–80.
- [37] E. Laperdrix, I. Justin, G. Costentin, O. Saur, J.C. Lavalley, A. Aboulayt, J.L. Ray, C. Nédéz, Appl. Catal. B. 17 (1998) 167–173.
- [38] H. Yu, B. Xue, P. Liu, J. Qiu, W. Wen, S. Zhang, H. Zhao, ACS Appl. Mater. Interfaces 4 (2012) 1289–1294.
- [39] P. Fleming, A. Farrell Richard, D. Holmes Justin, A. Morris Michael, J. Am. Ceram. Soc. 93 (2010) 1187–1194.
- [40] L. Nie, D. Mei, H. Xiong, B. Peng, Z. Ren, X.I.P. Hernandez, A. DeLaRiva, M. Wang, M.H. Engelhard, L. Kovarik, A.K. Datye, Y. Wang, Science 358 (2017) 1419.
- [41] J.-C. Lavalley, J. Travert, T. Chevreau, J. Lamotte, O. Saur, J. Chem. Soc. Chem. Commun. (1979) 146–148.